THE JOURNAL OF PHYSICAL CHEMISTRY A LETTERS

2006, *110,* 11384−11387
Published on Web 08/17/2006

Interferometric Coherence Transfer Modulations in Triply Vibrationally Enhanced Four-Wave Mixing

Mark A. Rickard, Andrei V. Pakoulev, Kathryn Kornau, Nathan A. Mathew, and John C. Wright*

Department of Chemistry, University of Wisconsin, Madison, Wisconsin 53706

Received: June 22, 2006

Triply vibrationally enhanced (TRIVE) four-wave mixing (FWM) spectroscopy in a mixed frequency/time domain experiment contains new output coherences that isolate nonlinear pathways that involve coherence transfer. Coherence transfer occurs when a thermal bath induces coupling between two states so a quantum mechanical entanglement of a pair of quantum states evolves to entangle a new pair of quantum states. The FWM includes several equivalent coherence pathways that interfere and create a temporal modulation of the output coherence that is a signature of coherence transfer. The transfer shifts the output coherence frequency and isolates coherence transfer pathways from the stronger FWM processes that form the basis of coherent multidimensional spectroscopy. The use of coherence transfer offers the opportunity for another form of coherent multidimensional spectroscopy where cross-peaks appear because of the coherence transfer between quantum states. Since this approach is based on frequency domain methods, it requires only short-term phase coherence during the excitation process so the method is not constrained to accessing the quantum states lying within the excitation pulse bandwidth.

Coherent multidimensional optical spectroscopy offers the capability for measuring the correlations between quantum states that result from inter- and intramolecular interactions.[1−3] These new methods are based on four-wave mixing (FWM) where three excitation pulses create entanglements between as many as four quantum states which are phase coherent and emit superradiant directional output beams defined by phase matching. Measuring the frequency dependence of all of the coherences created in the entanglement provides three-dimensional spectra with cross-peaks between quantum states that are coupled by intra- or intermolecular interactions. The frequency dependence can be measured in the frequency domain by scanning the excitation frequencies while monitoring the enhancement of the output intensity or in the time domain by Fourier transformation of the coherences' temporal phase. Measuring the temporal decay of the coherences and populations provides all of the relaxation dynamics of the system. The relaxation dynamics include population decay, dephasing, and coherence transfer.[4] Coherence transfer occurs when coupling between two states causes a quantum entanglement to evolve to a different entanglement without a loss in phase information.[5] Early studies of coherence transfer were compromised by the difficulty in discriminating between it and other coherent and incoherent relaxation processes.[6−9] Khalil et al. showed how 2D-IR spectroscopy could create a resolvable peak in a coherent multidimensional experiment that could only occur from coherence transfer.[10] Zanni showed that coherence transfer peaks were more important in a fifth-order 2D-IR experiment, both because higher order states have larger couplings and because they could occur with a single coherence transfer.[11]

In this Letter, we report how a mixed frequency/time domain triply vibrationally enhanced (TRIVE)[12−14] FWM experiment isolates coherence transfer events and resolves the quantum interferences and coherence pathways that are responsible for coherence transfer. A mode-locked Ti:sapphire oscillator/regenerative amplifier excites two independently tunable optical parametric amplifiers (pulse width of 900 fs, bandwidth of 20 cm^{-1}, frequencies ω_1 and ω_2). The bandwidth is narrow compared with frequency differences between the vibrational features observed in this work, so ω_1 and ω_2 excite single quantum states. The ω_2 beam is split to provide a third beam (ω_2'). The beams are identically polarized. All three beams are focused into the sample at appropriate angles for phase matching, $\vec{k}_{out} = \vec{k}_1 - \vec{k}_2 + \vec{k}_2'$, and the output is measured at ω_m with a monochromator (2 cm^{-1} resolution). The output from the driven nonlinear polarization occurs at $\omega_1 - \omega_2 + \omega_2'$, and the free induction decay polarization occurs at the frequency of the output coherence. We monitor the output intensity as a function of the ω_1, ω_2, and ω_m frequencies and the $\tau_{2'1}$ and τ_{21} time delays ($\tau_{ij} \equiv \tau_i - \tau_j$, where τ_i is the temporal position of the pulse with frequency ω_i). The sample is a 200 μm thick mixture of 10 mM bis(triphenylphosphine)dicarbonyl nickel, $Ni(CO)_2(PPh_3)_2$, and (triphenylphosphine)tricarbonyl nickel, $Ni(CO)_3(PPh_3)$, in benzene.[14] This paper focuses on a cross-peak in the two-dimensional spectrum where $(\omega_1, \omega_2) = (2003, 1943)$ cm^{-1} and $\omega_m = \omega_1$.[15] This cross-peak occurs when ω_1 and ω_2 are resonant with transitions to the symmetric (s) and asymmetric (a) stretch modes from the ground state (g) of $Ni(CO)_2(PPh_3)_2$. This cross-peak can be excited by four different coherence

* Corresponding author. E-mail: wright@chem.wisc.edu.

10.1021/jp063917e CCC: $33.50

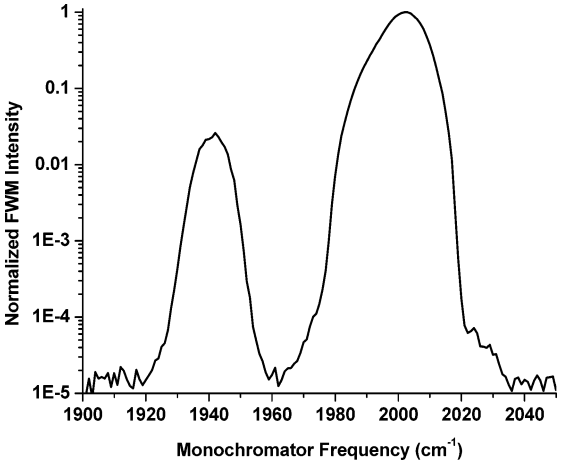

Figure 1. Logarithm of the FWM intensity as a function of the monochromator position when ($\omega_1 = 2003$, $\omega_2 = 1943$) cm^{-1}. The dominant peak is that expected by the normal FWM process, while the weaker peak can only arise from coherence transfer.

pathways that differ in the excitation pulses' time ordering:

$$\text{time ordering I:}\quad \text{gg} \xrightarrow{1} \text{sg} \xrightarrow{-2} \text{sa} \xrightarrow{2'} \text{sg}$$

$$\text{time ordering III:}\quad \text{gg} \xrightarrow{-2} \text{ga} \xrightarrow{1} \text{sa} \xrightarrow{2'} \text{sg}$$

$$\text{time ordering V:}\quad \text{gg} \xrightarrow{-2} \text{ga} \xrightarrow{2'} \text{gg} \xrightarrow{1} \text{sg}$$

$$\text{time ordering VI:}\quad \text{gg} \xrightarrow{2'} \text{ag} \xrightarrow{-2} \text{gg} \xrightarrow{1} \text{sg}$$

where the pair of letters represents the two quantum states that are entangled to form a particular coherence (we use the time ordering notation introduced in ref 12). Pathways III and V are rephasing pathways, and pathways I and VI are non-rephasing pathways. The boundary between pathways V and VI corresponds to a transient grating or traditional pump−probe experiment, the boundary between pathways III and V corresponds to a photon echo experiment, and region V corresponds to a stimulated photon echo experiment. Region III is fully coherent and involves no populations. Each pathway produces a sg output coherence that radiates at 2003 cm^{-1}, and indeed, that is the most intense output observed by the monochromator. However, Figure 1 shows an ω_m scan that reveals an output at 1943 cm^{-1}, the frequency of the ag coherence. This coherence can only be created by single coherence transfer.

Figure 2 shows a logarithmic two-dimensional scan of the time delays $\tau_{2'1}$ and τ_{21} while (ω_1, ω_2, ω_m) = (2003, 1943, 1943) cm^{-1}. The logarithmic scale allows one to observe the behavior over the entire dynamic range. The intensity is strongly modulated as a function of τ_{21}. Fourier transformation of the modulation shows that it corresponds to a frequency difference of 60 cm^{-1}, the frequency difference between the symmetric and asymmetric modes. It is strongest for time orderings III, V, and VI.

The coherence transfer pathways responsible for the behavior in Figures 1 and 2 are shown in Figure 3 for each of the relevant excitation pulse time orderings. Each pathway involves a single coherence transfer. In each case, the final coherence is the ag coherence that we observe. The multiple pathways creating the ag output coherence interfere with each other as a function of the delay times to produce the observed interference. As a specific example, consider the coherence pathway in time ordering III:

$$\text{gg} \xrightarrow{-2} \text{ga} \overset{\text{CT}}{\Rightarrow} \text{gs} \xrightarrow{1} \text{gg} \xrightarrow{2'} \text{ag}$$

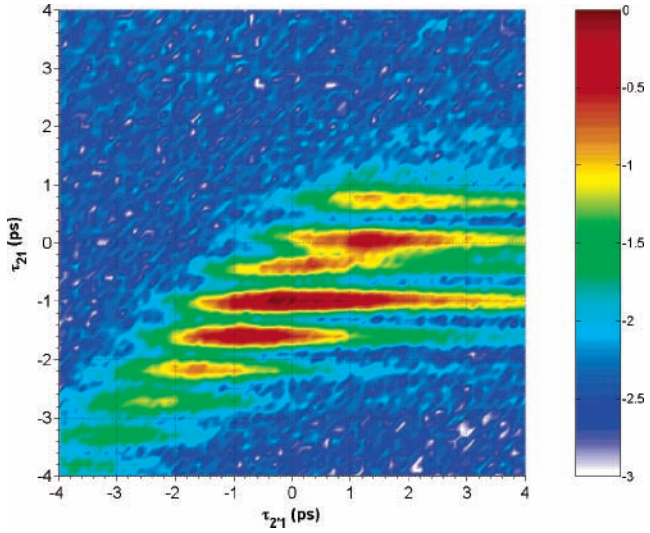

Figure 2. Dependence of the output intensity as a function of the delay times, $\tau_{2'1}$ and τ_{21}, between the three excitation pulses when ($\omega_1 = 2003$, $\omega_2 = 1943$, $\omega_m = 1943$) cm^{-1}. The time delays are defined as $\tau_{ij} \equiv t_i - t_j$, where i and j label the ω frequency.

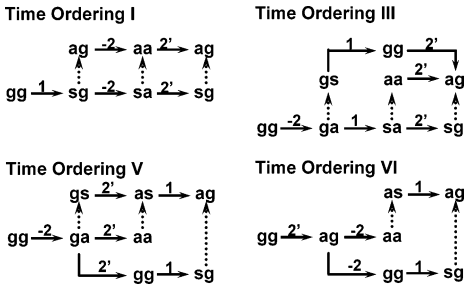

Figure 3. Liouville diagrams that show the flow of coherences and populations from the initial ground state population, gg, to the output coherence, ag, for each relevant time ordering. The phase matching is $\vec{k}_4 = \vec{k}_1 - \vec{k}_2 + \vec{k}_{2'}$. Dotted arrows represent coherence transfer, and solid arrows represent radiative transition induced by frequency ω_i.

Following the treatment of Stenholm,[7] the coherence transfer step is described by

$$\dot{\rho}_{gs} = (-i\omega_{gs} - \Gamma_{sg})\rho_{gs} + \kappa_{ga,gs}\rho_{ga} - \kappa_{gs,ga}\rho_{gs} \qquad (1)$$

where $\kappa_{ga,gs}$ is the Redfield rate constant for coherence transfer between the two coherences and $\kappa_{ga,gs}$ and $\kappa_{gs,ga}$ are related by detailed balance.[5] We assume the rate constants do not perturb the ga coherence, so we neglect $\kappa_{gs,ga}$ in finding ρ_{ga} and assume $\rho_{ga} \approx e^{(-i\omega_{ga} - \Gamma_{ag})t}$. We also neglect the effect of $\kappa_{gs,ga}$ on the ρ_{gs} dephasing rate. Solving eq 1,

$$\rho_{ga} \approx \frac{\kappa_{ga,gs}(e^{(-i\omega_{ga} - \Gamma_{ag})\tau_{12}} - e^{(-i\omega_{gs} - \Gamma_{sg})\tau_{12}})}{(i\omega_{as} + \Gamma_{gs} - \Gamma_{ga})} \qquad (2)$$

To emphasize the fundamental processes responsible for the observations, we make the simplest approximation. When we assume the impulsive, weak field, and Bloch limit without considering population dynamics or rephasing of the inhomogeneous broadening, we obtain the following expression for the ρ_{ag} output coherence when all time ordering III coherences are included (note that, for this time ordering, $\tau_{21} < 0$ and $\tau_{2'1} > 0$). We have factored out a common time dependent

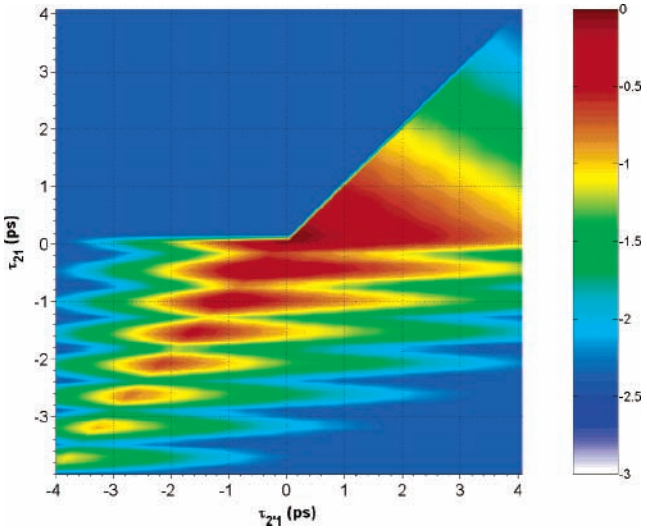

Figure 4. Simulation of Figure 2 in the impulsive limit using representative values for the coherence dephasing and population relaxation times. We neglect the effects of population dynamics and inhomogeneous broadening. For this simulation, the coherence dephasing times are 0.7 ps, the excited state population relaxation time is 2 ps, and the ground state recovery time is 20 ps. Fitting to Figure 2 requires inclusion of the finite pulse duration, the driven nonlinear polarization, population dynamics, and the rephasing dynamics associated with inhomogeneous broadening.

phase factor to emphasize the temporal dependence on the time delays.

$$\rho_{ag}^{III}(t) \approx e^{-i\omega_{sa}\tau_{12}-\Gamma_{ag}\tau_{12}-(i\omega_{ag}+\Gamma_{ag})(t-\tau_{2'2})}\left(\frac{\kappa_{ga,gs}e^{-\Gamma_{gg}\tau_{2'1}}}{i\omega_{as}+\Gamma_{sg}-\Gamma_{ag}}-\frac{\kappa_{gs,ga}e^{-\Gamma_{aa}\tau_{2'1}}}{i\omega_{as}+\Gamma_{aa}-\Gamma_{sa}}\right)+e^{-i\omega_{sa}\tau_{2'2}-\Gamma_{ag}\tau_{12}-\Gamma_{sa}\tau_{2'1}-(i\omega_{ag}+\Gamma_{ag})(t-\tau_{2'2})}\times\left(\frac{\kappa_{sa,aa}}{i\omega_{as}+\Gamma_{aa}-\Gamma_{sa}}-\frac{\kappa_{sg,ag}}{i\omega_{as}+\Gamma_{ag}-\Gamma_{sg}}\right)-e^{-\Gamma_{sg}\tau_{12}-\Gamma_{gg}\tau_{2'1}-(i\omega_{ag}+\Gamma_{ag})(t-\tau_{2'2})}\frac{\kappa_{ga,gs}}{i\omega_{as}+\Gamma_{gs}-\Gamma_{ga}} \quad (3)$$

Four of the five terms in this time ordering are paired, since they have the same delay-time dependence but opposite signs so they destructively interfere. The fifth term does not have a companion pathway because the ω_{sg} output frequency in the pathway

$$gg \xrightarrow{-2} ga \xrightarrow{1} sa \xrightarrow{2'} sg \overset{CT}{\Longrightarrow} ag$$

does not contribute, since the monochromator does not detect the modulation of the ag output coherence at ω_{sg}. If the monochromator was not used, this contribution would need to be included. The dephasing rates in the denominators are small in comparison with ω_{as}, while transfer rates such as $\kappa_{ga,gs}$ and $\kappa_{gs,ga}$ differ from each other by detailed balance. Transfer rates such as $\kappa_{sa,aa}$ and $\kappa_{sg,ag}$ should be similar, and terms involving them can cancel. The output intensity is proportional to $|\rho_{ag}(t)|^2$, so the intensity modulation will be controlled by cross-terms that heterodyne as a function of τ_{21} and reproduce the modulations in phase and frequency observed in Figure 3.

$$|\rho_{ag}^{III}(t)|^2 \approx |e^{-i\omega_{sa}\tau_{12}-\Gamma_{ag}\tau_{12}}(\kappa_{ga,gs}e^{-\Gamma_{gg}\tau_{2'1}}-\kappa_{gs,ga}e^{-\Gamma_{aa}\tau_{2'1}})-\kappa_{ga,gs}e^{-\Gamma_{sg}\tau_{12}-\Gamma_{gg}\tau_{2'1}}|^2 \quad (4)$$

The corresponding equations for the other relevant time orderings are shown below. Making similar simplifications, one can see that time orderings III, V, and VI predict modulations that depend on τ_{21}, while time ordering I has modulations only if the interference between pathways is incomplete. There are weaker modulations that depend on $\tau_{2'1}$ and $\tau_{2'2}$ that arise from incomplete cancellation.

$$\rho_{ag}^{I}(t) \approx e^{-i\omega_{sa}\tau_{21}-\Gamma_{sg}\tau_{21}-\Gamma_{aa}\tau_{2'2}-(i\omega_{ag}+\Gamma_{ag})(t-\tau_{2'1})}\times\left(\frac{\kappa_{sg,ag}}{i\omega_{as}+\Gamma_{ag}-\Gamma_{sg}}-\frac{\kappa_{sa,aa}}{i\omega_{as}+\Gamma_{aa}-\Gamma_{sa}}\right)+e^{-i\omega_{sa}\tau_{2'1}-\Gamma_{sg}\tau_{21}-\Gamma_{sa}\tau_{2'2}-(i\omega_{ag}+\Gamma_{ag})(t-\tau_{2'1})}\left(\frac{\kappa_{sa,aa}}{i\omega_{as}+\Gamma_{aa}-\Gamma_{sa}}-\frac{\kappa_{sg,ag}}{i\omega_{as}+\Gamma_{ag}-\Gamma_{sg}}\right)-e^{-\Gamma_{ag}\tau_{21}-\Gamma_{aa}\tau_{2'2}-(i\omega_{ag}+\Gamma_{ag})(t-\tau_{2'1})}\frac{\kappa_{sg,ag}}{i\omega_{as}+\Gamma_{ag}-\Gamma_{sg}} \quad (5)$$

$$\rho_{ag}^{V}(t) \approx e^{-i\omega_{sa}\tau_{2'2}-\Gamma_{ag}\tau_{2'2}-\Gamma_{ab}\tau_{12'}-(i\omega_{ag}+\Gamma_{ag})(t-\tau_{12})}\times\left(\frac{\kappa_{ga,gs}}{i\omega_{as}+\Gamma_{sg}-\Gamma_{ag}}-\frac{\kappa_{aa,as}}{i\omega_{as}+\Gamma_{as}-\Gamma_{aa}}\right)+e^{-i\omega_{sa}\tau_{12}-\Gamma_{ag}\tau_{2'2}-(i\omega_{ag}+\Gamma_{ag})(t-\tau_{12})}\left(\frac{\kappa_{aa,as}e^{-\Gamma_{aa}\tau_{12'}}}{i\omega_{as}+\Gamma_{as}-\Gamma_{aa}}-\frac{\kappa_{sg,ag}e^{-\Gamma_{gg}\tau_{12'}}}{i\omega_{as}+\Gamma_{ag}-\Gamma_{sg}}\right)-e^{-\Gamma_{sg}\tau_{2'2}-\Gamma_{as}\tau_{12'}-(i\omega_{ag}+\Gamma_{ag})(t-\tau_{12})}\frac{\kappa_{ga,gs}}{i\omega_{as}+\Gamma_{sg}-\Gamma_{ag}} \quad (6)$$

$$\rho_{ag}^{VI}(t) \approx e^{-i\omega_{sa}\tau_{12'}-\Gamma_{ag}\tau_{22'}-(i\omega_{ag}+\Gamma_{ag})(t-\tau_{12'})}\left(\frac{\kappa_{aa,as}e^{-\Gamma_{aa}\tau_{12}}}{i\omega_{as}+\Gamma_{as}-\Gamma_{aa}}-\frac{\kappa_{sg,ag}e^{-\Gamma_{gg}\tau_{12}}}{i\omega_{as}+\Gamma_{ag}-\Gamma_{sg}}\right)-e^{-i\omega_{sa}\tau_{22'}-\Gamma_{ag}\tau_{22'}-\Gamma_{ba}\tau_{12}-(i\omega_{ag}+\Gamma_{ag})(t-\tau_{12'})}\frac{\kappa_{aa\_as}}{i\omega_{as}+\Gamma_{as}-\Gamma_{aa}} \quad (7)$$

Figure 4 shows the results of a simulation that includes all of the time orderings and coherence transfer pathways shown in Figure 3 in the impulsive limit. We assume the transfer rates in all of the pathways are defined only by detailed balance, and we neglect pathways that involve more than one coherence transfer or population relaxation. The simulation reproduces the character, relative intensities, and time durations of the modulations observed in the experimental data. The dephasing and population transfer rates can be obtained for all the coherences and populations by a more complete simulation that includes the finite width of the excitation pulses, the effects of inhomogeneous broadening and rephasing, and the full population dynamics. The finite pulse duration is particularly important in the regions of pulse overlap where both driven and free induction decay dominate and the different time ordered coherence pathways overlap.

Kahlil et al. attributed their coherence transfer peak to processes involving two coherence transfers because the transition moments in their experiment were perpendicular and single coherence transfer should not be observable.[10] Our experiments clearly must involve single coherence transfer because there are no double coherence transfer pathways that predict the observed

behaviors. The $Ni(CO)_2(PPh_3)_2$ molecule in this study has a different geometry and normal modes than the rhodium chelate used by Kahlil et al. and avoids the constraints of the rhodium chelate.[10] Since the experimental results clearly show that the coherence transfer occurs once, the transition moments must have a common component that can produce a coherent output with the parallel polarization geometry used in this work.

It is important to note that the full width at half-maximum (fwhm) for a single peak in the coherence transfer modulation is 250 fs, considerably shorter than the 900 fs excitation pulse width. In each pathway shown in Figure 3, the coherence created by coherence transfer has two oscillation frequencies. The observed temporal modulation results from interference between the different coherence transfer pathways that cause self-heterodyning to form the observed beat. The time scale for the beating is defined by the interference between pathways and not by the excitation pulse. It is also important to note that the beating continues over longer time scales in Figures 2 and 4 than the coherences' dephasing times because the phase modulation is stored in intermediate populations and zero quantum coherences (e.g., ba in Figure 3) with longer lifetimes.

Coherence transfer provides a mechanism for a third form of fully coherent multidimensional spectroscopy. FWM spectroscopies such as doubly vibrationally enhanced (DOVE) FWM use two infrared transitions to excite two coupled vibrational states and a Raman transition between the two coupled states. Cross-peaks in DOVE FWM require that one of the three transitions be a combination band.[16] FWM spectroscopies such as 2D-IR and TRIVE require four infrared transitions. Cross-peaks require anharmonicities that shift the combination band or overtone or change their relaxation dynamics so the destructive interference between the pathways involving the fundamentals and the pathways involving the combination bands is incomplete.[13,17] Coherence transfer provides a third mechanism for creating cross-peaks in fully coherent multidimensional spectroscopy that have distinct advantages because the output frequencies are shifted from those expected from driven processes and because the temporal and spectral features in this form of spectroscopy define the quantum states that are coupled and their coherent dynamics. The dynamics includes interference effects that are signatures of coherence transfer. The time scale for this form of coherent spectroscopy is defined by the loss of coherence from the phased array of oscillators that create the output signal. This mixed frequency/time domain spectroscopy also avoids the need for long-term phase stability between excitation pulses with different frequencies, since the phase relationships are only required during a single excitation sequence.

Acknowledgment. This work was supported by the National Science Foundation under grant CHE-0130947. Acknowledgment is also made to the donors of the Petroleum Research Fund of the American Chemical Society for their support of this research.

References and Notes

(1) Mukamel, S. *Annu. Rev. Phys. Chem.* **2000**, *51*, 691.
(2) Wright, J. C.; Zhao, W.; Murdoch, K. M.; Besemann, D. M.; Condon, N. J.; Meyer, K. A. Nonlinear 2D Vibrational Spectroscopy. In *Handbook of Vibrational Spectroscopy*; Chambers, J. M., Griffiths, P. R., Eds.; John Wiley and Sons: New York, 2001.
(3) Jonas, D. M. *Annu. Rev. Phys. Chem.* **2003**, *54*, 425.
(4) Jean, J. M.; Friesner, R. A.; Fleming, G. R. *J. Chem. Phys.* **1992**, *96*, 5827.
(5) Redfield, A. G. *Adv. Magn. Reson.* **1965**, *1*, 1.
(6) Berman, P. R. *Phys. Rev. A* **1995**, *51*, 592.
(7) Stenholm, S. *J. Phys. B* **1977**, *10*, 761.
(8) Ohtsuki, Y.; Fujimura, Y. *J. Chem. Phys.* **1989**, *91*, 3903.
(9) Bree, P. D.; Wiersma, D. A. *J. Chem. Phys.* **1979**, *70*, 790.
(10) Khalil, M.; Demirdoven, N.; Tokmakoff, A. *J. Chem. Phys.* **2004**, *121*, 362.
(11) Ding, F.; Fulmer, E. C.; Zanni, M. T. *J. Chem. Phys.* **2005**, *123*.
(12) Meyer, K. A.; Thompson, D. E.; Wright, J. C. *J. Phys. Chem. B* **2004**, *108*, 11485.
(13) Besemann, D. M.; Meyer, K. A.; Wright, J. C. *J. Phys. Chem. B* **2004**, *108*, 10493.
(14) Meyer, K. A.; Wright, J. C. *Chem. Phys. Lett.* **2003**, *381*, 642.
(15) Pakoulev, A. V.; Rickard, M. A.; Meyers, K. A.; Kornu, K.; Mathew, N. A.; Thompson, D. C.; Wright, J. C. *J. Phys. Chem. B* **2006**, *110*, 3352.
(16) Zhao, W.; Wright, J. C. *Phys. Rev. Lett.* **2000**, *84*, 1411.
(17) Tokmakoff, A. *J. Phys. Chem. A* **2000**, *104*, 4247.